CFD Simulation and Investigation of Slurry Flows in Pipeline

Marwane ElKarii

Mines ParisTech, CES, Paris, France

Mohammed VI Polytechnic University (UM6P), MSDA, Ben Guerir, Morocco

Octorber 2021

Contents

1 Introduction **2**

1.1 CFD approaches for multiphase flows 3

1.2 Problem Description 4

2 Literature Review : slurry pipes modeling and simulation **6**

3 Theoretical and empirical models **13**

3.1 Mathematical models 13

3.2 Pressure drop calculations 18

3.3 Turbulence model 19

3.4 Near-wall treatment 20

3.5 Methodology 20

4 Results and discussions **22**

4.1 Single phase flow 22

4.2 Two phase flow 26

4.3 Surrogate model 31

5 Conclusion **35**

Chapter 1

Introduction

Pipeline transport of solid-liquid sludge is an essential operation in many areas, such as mining and chemical processing. This comes down to the fact that pipelines are more efficient and environmentally friendly than railway transportation. Yet, the transported fluid may be highly viscous and have complex rheology. Moreover, the flow within the pipe is generally highly turbulent and complex (Lahiri and Ghanta [2010]) and problems like pipe plugging, and solid sedimentation could occur. Therefore, to ensure a continuous and optimal flow, different parameters should be controlled. In particular, the distribution of solids and the pressure drop within the pipeline represent a serious concerns to engineers, since their determination involves considerable technical difficulties. Thus, having means to predict the physics of the slurry flow is essential for the control of the pipeline process. The rapid increase in computational power has made it possible to widely distribute different tools and techniques, capable of modeling complex flows in real-dimensional geometries. This paved for a better handling of such flows by complementing empirical methods with digital simulations. Therefore, Computational Fluid Dynamics (CFD) has appeared as an effective tool to model and predict unknown or particular slurry flow scenarios (Bin and DaWen [2002]), and it can provide a series of monitoring information, which is difficult to achieve by experience alone. The advantages of CFD can be categorized as

- It provides a detailed understanding of flow distribution, mass and heat transfer, particulate separation, etc. Consequently, all these will lead to a much better and deeper understanding of what is happening in a particular process or system.
- It is able to reduce scale-up problems because the models are based on fundamental physics and are scale independent.
- It is particularly useful in simulating conditions where it is not possible to take detailed measurements.

1.1 CFD approaches for multiphase flows

Generally, the CFD approaches for the simulation of slurry flows can be classified into:

- Eulerian-Lagrangian approaches (Crowe et al. [2011]), where the liquid phase is modeled as a continuum and solved in an Eulerian cell-based framework, whereas the behavior of the solid phase is obtained by the Discrete Particle Method (DPM), in which the individual trajectories of computational particles are calculated in a Lagrangian fashion.
- Eulerian-Eulerian approaches (Crowe et al. [2011]), where both phases are modeled as interpenetrating continua, and two sets of conservation equations are solved jointly in the Eulerian framework. The coupling between the two phases depends on the amount of solids in the flow, and it ranges from one-way coupling for dilute slurries (*i.e.*, the particles do not affect the liquid flow field) to four-way coupling for dense slurries (where the particle-particle and particle-fluid interactions are important as well). This approach characterizes the majority of the earlier CFD investigations of slurry pipe flows which provides a good compromise between accuracy and computational cost. Yet three models are possible within this approach.

Table 1.1 shows a comparison of the latter models. [1]

[1] Particle-laden flow = Particle charge flows refer to a two-phase flow in which one of the phases is continuously connected and the other phase consists of small immiscible particles and typically diluted.

Table 1.1: Comparison between Euler-Euler models

VOF	Mixture Model	Multi-phase Eulerian Model
Modelling non-miscible fluid	Model used if there is a wide distribution of dispersed phases	Interphase laws available.
A single set of motion equations	Interphase laws not available	More precise.
Examples: free surface flow (Jing et al. [2016])), large bubbles in a liquid (Al-Yaari and Abu-Sharkh [2011])), stratified flow (Akhtar et al. [2007]))	Examples: particle-laden flow* with low load (Dufek and Bergantz [2007]), bubble flow, sludge flow (Chen et al. [2009])	Examples: sludge flow (Ofei and Ismail [2016]), sedimentation ((Gopaliya and Kaushal [2016]), fluidized beds (Ofei et al. [2014])).

1.2 Problem Description

This work concerns the transport of phosphate ores in the context of an industry 4.0. The process begins with the extraction of ore that is transported as pulp (Water + Phosphate) in a pipe (pipeline), from the mine to the industrial units for processing (cf. Fig. 1.1). This pulp is characterized by a solid volume concentration that goes up

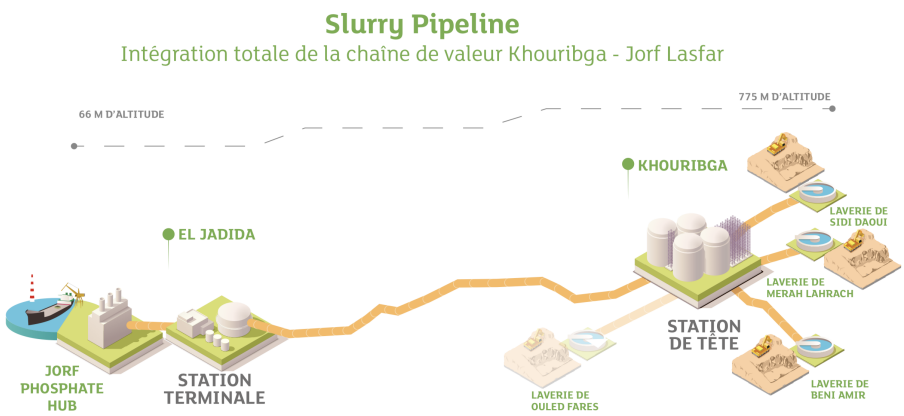

Figure 1.1: Transport process of phosphate slurry

to 40 %, it contains rigid solid particles of random shapes having an equivalent spherical diameter ranging from 44 μm to 400 μm. The ore particles are characterized by an average total porosity of 20 % by volume, then an effective density of 2600 kg/m^3 when the pores are filled with water. The operation of the phosphate slurry pipe is controlled by a series of pressure and choke stations. The pipeline receives the phosphate ore, of different qualities, from four different washing stations, which gives it variable flow

properties (viscosity, density, speed, pressure...). The phosphate pulp is transported in batches, separated by batches of water to control the quality and flow of the pulp (cf. Fig. 1.2).

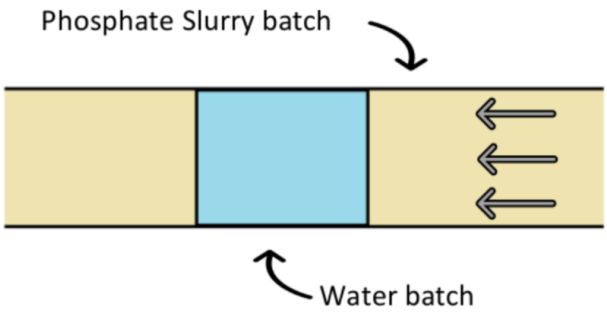

Figure 1.2: Phosphate slurry flow

The main challenge of the work to be carried out in the context of this thesis is is to set the basis for an intelligent control for the transport process, based on computational fluid dynamics (CFD) simulation models. This system will ensure optimal operation of the process, predict the evolution of certain critical parameters and contribute to operational decision-making. From an application point of view, among the industrial stakes of the project of this thesis:

- Increase productivity (volume sent by the pipe);
- Secure the pipe by mastering the characteristics of the pulp;
- Predict solid concentration profiles and pressure losses in the pipeline;
- Optimize pipe operation according to pulp quality;
- Optimize energy consumption, etc;

Chapter 2

Literature Review : slurry pipes modeling and simulation

A summary of the most relevant numerical studies on slurry flows in horizontal pipes published so far are reported, alongside with the adopted modelling approach. Beginning with Eulerian-Lagrangian approach, this latter was employed for this kind of applications for sand-water slurry by Capecelatro and Desjardins [2013], where the Large Eddy Simulation (LES) method Versteeg and Malalasekera [2007] has been used to simulate the turbulent flow of the liquid phase, while the solid phase was treated by DPM. Arolla and Desjardins [2015] used the same numerical setup to characterize a sand-water flow pattern for increasing values of liquid superficial velocity. Always in the Eulerian-Lagrangian approach but this time it was employed with different characteristics such as transportation of coarse NaCl particles in brine by Uzi and Levy [2017], where the liquid phase is handled by a computationally cheaper Reynolds-Average Navier-Stokes (RANS) technique, to examine the effects of the operating conditions on the flow. Concerning the mixture model, Ling et al. [2003] performed CFD simulations for sand-water slurry flows through horizontal pipes, where a simplified 3D algebraic slip mixture (ASM) model is introduced along with RNG k–ϵ turbulent model to obtain the precise numerical solution in fully developed turbulent flow. They compared

CFD results of mean pressure gradients with experimental results, and found a big discrepancy between them takes place when the mean velocities of slurry flows are lower than corresponding critical deposition velocities. Lin and Ebadian [2008] numerically investigated sand–water slurry flows in the entrance region of horizontal pipe, again using ASM model, and have focused mainly on illustrating and comparing the developing processes of various flow parameters. Silva et al. [2016] performed simulations for Saline Water-Glass beads slurry using Mixture Model coupled with a High Reynolds k–ϵ turbulence model, results were validated with data attained with an Electrical tomography apparatus. The model produced accurate representations for the highest flow rates, while showing some deviations for the lower flow rate. However, the majority of the earlier CFD investigations of slurry pipe flows were performed using the Two Fluid Model. In most TFMs, constitutive equations for the solid phase derived from the Kinetic Theory of Granular Flow (KTGF) were employed. The most relevant numerical studies on slurry flows in horizontal pipes published so far, the study of Hernandez et al. [2008] for sand-water slurry, where homogeneous and heterogeneous flow regimes without bed were considered along with predictions of pressure gradients at the fully developed zone. Ekambara et al. [2009] investigated the effect of in situ solids volume concentration, particle size, mixture velocity, and pipe diameter, on local time-averaged solids concentration profiles, particle and liquid velocity profiles, and frictional pressure loss. Excellent agreement between the predicted and the experimental was obtained. Chen et al. [2009] used the same numerical configuration to simulate flow of coal-water slurries (CWS) in a horizontal pipeline, with bimodal distribution for coal particles. They found out that the simulation results of the binary solid phase model is closer to experimental data, as compared to the results of the single solid phase model. Bossio et al. [2009] focused on modeling of non-Newtonian Laterite-Sand slurry where the mean pressure gradients were compared with experimental data. Antaya et al. [2012] performed simulations for concentrated mixtures of sand-water slurry with mono-sized and bimodal particle sizes. Shear stress model (SST) was tested in addition to the k–ϵ model to treat the turbulence of the continuous phase. Success

has been achieved in the use of k–ϵ model, with the SST model being superior, especially in the near-wall region. However Kaushal et al. [2012], tried both Mixture and two-phase model to simulate mono-dispersed fine particles at high concentration of glass beads mixed with water. They proved again the failure of the Mixture Model predictions at high velocities and high solid concentrations compared to TFM. Jiang and Zhang [2012] worked on an unusual type of slurry flows which is Slush nitrogen flow using the 2D Eulerian – Eulerian multiphase approach. The per-phase k–ϵ turbulence model is used in the study to model the turbulent two-phase flow. The effects of the flow velocity and the mean solid volume fraction on the flow characteristics of slush nitrogen are investigated numerically in this study. The same team in very next year Jiang and Zhang [2013] investigated the same slush and nitrogen flow. Based on the experimental and numerical results they distinguished three flow patterns, which for each one they had studied the variation of pressure drop. They obtained the general correlation of the friction factor with the slush Reynolds number of slush nitrogen with various solid volume fractions. Wang et al. [2013] applied the two fluid model to describe an ice slurry flow without considering ice melting. After validation of the model with experimental data, it was used to investigate the distributions of ice slurry flow, ice particle concentration and pressure drop in horizontal, vertical and 90 elbow pipes respectively. They found that for pressure drop, the numerical model is found being able to provide results in good agreement with the experimental data where the relative errors are limited to 20%. Messa et al. [2013] developed a new two-fluid model for the simulation of Sand and Glass beads Water slurry. Contrary to previous works with TFM models, they did not integrate the kinetic theory of granular flows to determine solid viscosity. They studied the effect of the wall boundary condition for the solid phase on the pressure gradient, where they found that the best match between measurements and computations is obtained when the equilibrium logarithmic law of Launder and Spalding for smooth walls is applied to the solid phase. Then, Messa et al. [2014] used the new TFM model to simulate a fully-suspended Sand-Water slurry flow in horizontal pipes and bends. They claimed that the model is robust and numerically

stable, and requires relatively short computer time to provide a converged steady-state solution. The novelty of the proposed model and its better performance compared to similar ones reside in the method of accounting for some key physical mechanisms governing these flows, namely turbulent dispersion, interphase friction, and viscous and mechanical contributions to friction. Messa and Malavasi [2015] further modified Messa et al. [2014] model by incorporating a new wall boundary condition for the solid phase, a more general correlation for the viscosity of the slurry, accounting for particle shape along with a different solution algorithm. These changes resulted in low computational effort with improved performance. They verified the modified model by comparing its outcomes with experimental results for sand-water slurries available in the literature. returning to the TFM combined with KTGF, Gopaliya and Kaushal [2015] studied the effects of grain size on various Sand-Water slurry flow parameters. They found that at the same volumetric concentration, pressure drop increases with increase in grain size. Hashemi et al. [2016] performed experiments in a 265 mm diameter pipe loop with sand-in-water slurries, then selected experimental conditions were numerically simulated using a commercial CFD package, ANSYS CFX. They noticed that the agreement between the numerical results and the experimental data is concentration dependent, with relatively closer agreement at lower concentrations. Kumar et al. [2017] presented experimental data of iron-ore slurry flow cases through 105 mm pipe, the obtained results are validated using TFM-KTGF model. Results reflect good resemblance between measured and predicted pressure drops, solid concentrations and velocity profiles. Singh et al. [2017] investigated the flow characteristics of coal water slurry having high solid concentrations in slurry pipeline. They have noticed that the coal-water slurry shows Newtonian behaviour at 30% solid concentration (by-weight) and beyond this it depicts non Newtonian pseudo plastic behavior. In this study also SST k-ω turbulence model was found a better predictor over other models namely Standard k-ϵ, RNG k-ϵ, Realizable k-ϵ and Standard k-ω models. A year after Li et al. [2018b] developed a useful three-dimensional multiphase hydrodynamic model based on the kinetic theory of granular flow, for simulating multi-sized glass beads-water slurry

transport through pipelines, to investigate the distributions of solid concentration, flow velocity, granular pressure, and wall shear stress. The simulation results of different-sized particle behaviors in multi-sized slurry has significant reference value. Li et al. [2018a] also in the same year studied the effect of interaction of particles with different sizes on particle kinetics in multi-sized slurry, first they concluded that the increase of speed of resistance in a graded slurry is more gradual than in a single-sized slurry with the same conditions as the solid concentration increases, then they found that the wall shear stress of coarse particles is significantly reduced by the existence of fine particles with increasing flow rate and solid concentration, and finally they affirmed that the existence of fine particles significantly reduces the collision intensity of coarse particles and velocity fluctuations in the multi-sized slurry.

Summary on models classification

Following the literature review presented above, our CFD approach will be based on the Eulerian model (Two Fluid Model) as it is the most complete model and the most used one to deal with suspensions transport issues, and is confirmed to be the most accurate and gives generally good results. While mixture model fails to predict pressure drops correctly and the amount of error increases rapidly with the slurry concentration (Kaushal et al. [2012]). The main conclusions from the literature review are summed in table 2. The description of the TFM model is given in section 3.1. The dynamics of the solid phase is modeled by the KTGF to consider both particle collisions and frictions. Also, based on the previously cited works, the turbulence of the continuous phase is treated by the k-ϵ based models, that generally shows reasonable robustness, and give reasonable accuracy for a wide range of applications. Yet, even though success is usually achieved using models based on the k-epsilon, it should be made clear that they may not perform well in the region near the wall (Antaya et al. [2012]). Therefore, a near-wall treatment model is presented in section 3.4, to address the weak performance of the choosed turbulence models in this area of the pipe. See Table 2.1 for a summary on model classification.

DPM (Eulerian-Lagrangian Appraoch)	The discrete phase must be present at a fairly low volume fraction, usually less than 10-12%
Mixture Model	There is a big discrepancy between CFD results with experimental, especially at lower flow rates
TFM Model	TFM is accurate and gives generally good results comparing to the mixture model. TFM results are better and closer to the experimental data in the case of bimodal particle sizes or at higher velocities.

Table 2.1: Summary on models classification

In fact, modern modeling strategies, for industrial processes, integrates usually 3D simulation techniques using computational fluid dynamics (CFD) and/or discrete element methods (DEM). These 3D models are then integrated as surrogate models that can be used in operations simulation and monitoring tools (Decision Support Systems). Classically, response surface methodologies (RSM) are applied to build a polynomial surrogate model (Rabhi et al. [2018]), but also in recent works machine leaning techniques such as artificial neural networks (ANN) can be used (Seong et al. [2020]). The current modeling approach consists of constructing 3D models for different type of pipe elements (horizontal, inclined, bended pipes), and then use them to construct surrogates that models the pressure drop within each element. Such models can then be used in dynamical models for monitoring slurry pipe systems and to conduct sizing studies to cover variations in the operation conditions like inlet pressure and inlet flow rate. This approach will first be applied to a single fluid flow to validate the approach of constructing a surrogate pressure drop model through 3D numerical simulation, and then to slurry flows with solid volume fraction corresponding to the applications that are aimed to cover.

A parametric analysis is conducted to investigate the impact of the variation in the particle size, solids concentration, and inlet velocity, on the solid concentration profile, the solid velocity profile and finally their effect on the variation in the pressure drop along the pipe. This analysis allows us to validates our simulations for turbulent slurry flows versus experimental data. The data used in this work is regarding a horizontal

pipe case for Water-Sand slurry flow: transported solid volume fraction between 19 % and 45 %; velocities between 1 m/s and 8.0 m/s; and particles sizes of 90 μ_m and 270 μ_m.

Chapter 3

Theoretical and empirical models

3.1 Mathematical models

In the two-fluid Eulerian-Eulerian approach, each phase is described by a set of averaged conservation equations. The present formulation follows Elkarii et al. [2020], Passalacqua and Fox [2011]. A general discussion of how such models are derived via averaging can be found in Drew and Passman [2006]. Introducing the particle volume fraction field ϕ, the governing equations for the two phases are expressed as follows

$$\begin{cases} \partial_t \left(\varrho_{\mathfrak{f}} \phi_{\mathfrak{f}}\right) + \partial_i \left(\varrho_{\mathfrak{f}} \mathfrak{u}_{\mathfrak{p},i} \phi_{\mathfrak{f}}\right) = 0, \\ \varrho_{\mathfrak{f}} \phi_{\mathfrak{f}} \left(\partial_t \mathfrak{u}_{\mathfrak{f},i} + \mathfrak{u}_{\mathfrak{f},j} \partial_j \mathfrak{u}_{\mathfrak{f},i}\right) = \varrho_{\mathfrak{f}} \phi_{\mathfrak{f}} g_i - \phi_{\mathfrak{f}} \partial_i \mathfrak{p} + \partial_j \tau_{\mathfrak{f},ij} + \mathrm{F}_{\mathfrak{f},i}, \end{cases} \tag{3.1}$$

where the letter t represents the time and the symbols ∂_t and ∂_i denote the partial differential operators ∂/∂_t and $\partial/\partial x_i$, respectively. Furthermore, the summation convention for repeated indices is used. Here, $\phi_{\mathfrak{f}}$ is the volume fraction and $\varrho_{\mathfrak{f}}$ the density of the respective fluid. The velocity vector is denoted by $\boldsymbol{\mathfrak{u}}_{\mathfrak{f}}$, the pressure by $\mathfrak{p}$, and the gravity by $\boldsymbol{g}$. The index $\mathfrak{f}$ is symbolic for the solid and the fluid phase, e.g. the solid phase fraction may be denoted by $\phi_{\mathfrak{p}}$, the one of the continuous phase as $\phi_{\mathfrak{w}}$. The sum of the volume fraction of the different phases is always unity. The stress tensor is evaluated as $\tau_{\mathfrak{f},ij} = 2\phi_{\mathfrak{f}}\mu_{\mathfrak{f}} \left(\mathcal{S}_{\mathfrak{f},ij} - \mathcal{S}_{\mathfrak{f},kk}\delta_{ij}/3\right)$ with $\mathcal{S}_{ij} = \left(\partial_j \mathfrak{u}_{\mathfrak{f},i} + \partial_i \mathfrak{u}_{\mathfrak{f},j}\right)/2$. The last term

$\mathbf{F}_{\mathfrak{f}}$ in (3.1) denotes the momentum transfer between the phases. It is decomposed into drag forces $\mathbf{F}_{\mathfrak{f}}^{\mathrm{d}}$, lift forces $\mathbf{F}_{\mathfrak{f}}^{\mathrm{l}}$, and turbulent dispersion forces $\mathbf{F}_{\mathfrak{f}}^{\mathrm{vm}}$ and it is expressed therefore as

$$\mathbf{F}_{\mathfrak{f},i} = \mathbf{F}_{\mathfrak{f}}^{\mathrm{d}} + \mathbf{F}_{\mathfrak{f}}^{\mathrm{l}} + \mathbf{F}_{\mathfrak{f}}^{\mathrm{vm}}. \tag{3.2}$$

In the present two-fluid calculation, the following functional forms Maxey and Riley [1983] are retained

$$\begin{cases} \mathbf{F}_{\mathfrak{f}}^{\mathrm{d}} = \frac{3}{4}\frac{\varrho_{\mathfrak{w}}}{\mathrm{d}_{\mathfrak{s}}}\mathcal{C}_{\mathrm{d}}\|\mathbf{u}_{\mathfrak{w}} - \mathbf{u}_{\mathfrak{s}}\|\left(\mathbf{u}_{\mathfrak{w}} - \mathbf{u}_{\mathfrak{s}}\right), \\ \mathbf{F}_{\mathfrak{f}}^{\mathrm{l}} = \varrho_{\mathfrak{w}}\mathcal{C}_{\mathrm{l}}(\mathbf{u}_{\mathfrak{w}} - \mathbf{u}_{\mathfrak{s}}) \times (\nabla \times \mathbf{u}_{\mathfrak{w}}), \\ \mathbf{F}_{\mathfrak{f}}^{\mathrm{vm}} = \varrho_{\mathfrak{w}}\mathcal{C}_{\mathrm{vm}}\left(\mathrm{D}_t^{\mathfrak{w}}\mathbf{u}_{\mathfrak{w}} - \mathrm{D}_t^{\mathfrak{s}}\mathbf{u}_{\mathfrak{s}}\right), \end{cases} \tag{3.3}$$

where $\mathrm{D}_t^{\mathfrak{f}} = \partial_t + \mathrm{u}_{\mathfrak{f},j}\partial_i$ stands for the substantive derivative corresponding to each phase $\mathfrak{f}$, and $\mathcal{C}_{\mathrm{d}}$, $\mathcal{C}_{\mathrm{l}}$ and $\mathcal{C}_{\mathrm{vm}}$ are the drag, lift and virtual mass coefficients, respectively. For the drag coefficient, the solid particle drag model of Wen and Yu [1966] is retained, which reads

$$\mathcal{C}_{\mathrm{d}} = \begin{cases} \frac{24}{\mathcal{R}\mathfrak{e}}\left(1 + 0.15\mathcal{R}\mathfrak{e}^{0.687}\right)\left(1 - \phi_{\mathfrak{s}}\right)^{-2.7} & \text{, if } \mathcal{R}\mathfrak{e} \leq 10^3, \\ 0.44\left(1 - \phi_{\mathfrak{s}}\right)^{-2.7} & \text{, if } \mathcal{R}\mathfrak{e} \geq 10^3, \end{cases} \tag{3.4}$$

where $\mathcal{R}\mathfrak{e} = \varrho_{\mathfrak{s}}\|\mathrm{u}_{\mathfrak{r}}\|\mathrm{d}_{\mathfrak{s}}/\mu_{\mathfrak{s}}$ is the Reynolds number bases on the particle diameter $\mathrm{d}_{\mathfrak{s}}$ and the relative velocity $\mathbf{u}_{\mathfrak{r}} = \mathbf{u}_{\mathfrak{w}} - \mathbf{u}_{\mathfrak{s}}$. For virtual mass coefficient $\mathcal{C}_{\mathrm{d}}$, a fixed value of 0.5 is used throughout the present study Auton et al. [1988]. The solid phase is modelled in this Eulerian framework as an interpenetrating fluid but with a viscosity that is determined by the kinetic theory of granular flows.

Solid-phase viscosity

Solid-phase viscosity is determined using Kinetic Theory of Granular flows(KTFG) which is based on the kinetic theory of gases in a generalized way to take into account collisions of inelastic particles to define a granular temperature θ in solid phase which directly affects the phase stress tensor (González et al. [2017]). Analogical to the

thermodynamic temperature for gases, the granular temperature Θ was introduced as a measure for the energy of the fluctuating velocity of the particles. The equation of conservation of solids fluctuating energy can be expressed as Wang et al. [2013]:

$$\frac{3}{2}\left[\partial_t\left(\alpha_{\mathfrak{s}}\varrho_s\Theta_{\mathfrak{s},i}\right)+\partial_i\left(\alpha_{\mathfrak{s}}\varrho_{\mathfrak{s}}\mathfrak{u}_{\mathfrak{s},i}\Theta_{\mathfrak{s}}\right)\right]=\underbrace{\partial_i\left(-\mathfrak{p}_{\mathfrak{s}}\mathfrak{u}_{\mathfrak{s},i}+\mathfrak{u}_{\mathfrak{s},i}\tau_{\mathfrak{s},ij}\right)}_{\mathcal{T}_1}+\underbrace{\partial_i\left(\kappa_\Theta\partial_i\Theta_i\right)}_{\mathcal{T}_2}-\underbrace{\gamma_{\Theta_S}}_{\mathcal{T}_3}+\underbrace{\Phi_{\mathrm{LS}}}_{\mathcal{T}_4} \tag{3.5}$$

where the term $\mathcal{T}_1$ stands for the production term due to shear stress, $\mathcal{T}_2$ for diffusion, $\mathcal{T}_3$ for dissipation due to inelastic collisions, and $\mathcal{T}_4$ for tthe term responsible for dissipation/droduction due to the interaction with the carrier. Rather than solving the complete granular energy balance given in Eq. 3.5, Ekambara et al. [2009] assume the granular energy is in a steady state and dissipated locally and neglect convection and diffusion. Retaining only the generation and the dissipation terms, Eq. 3.5 simplifies to an algebraic expression for the granular temperature:

$$\partial_i\left(-\mathfrak{p}_{\mathfrak{s}}\mathfrak{u}_{\mathfrak{s},i}+\mathfrak{u}_{\mathfrak{s},i}\tau_{\mathfrak{s},ij}\right)-\gamma_{\Theta_S}+\Phi_{\mathrm{LS}}=0 \tag{3.6}$$

Expression for all the terms can be derived (Gidaspow [1994]):

$$\begin{cases}\gamma_{\Theta_{\mathfrak{s}}}=\frac{12\left(1-e^2\right)g_0}{d_{\mathfrak{s}}\sqrt{\pi}}\varrho_{\mathfrak{s}}\alpha_{\mathfrak{s}}^2\Theta_{\mathfrak{s}}^{3/2}\\ \Phi_{\mathrm{LS}}=-3\mathrm{K}_{\mathrm{SL}}\Theta_{\mathfrak{s}}\\ \mathfrak{p}_{\mathfrak{s}}=\alpha_{\mathfrak{s}}\varrho_{\mathfrak{s}}\Theta_{\mathfrak{s}}+2\varrho_{\mathfrak{s}}\left(1+e\right)\alpha_{\mathfrak{s}}^2g_0\Theta_{\mathfrak{s}}\end{cases} \tag{3.7}$$

where e is the coefficient of restitution for particle collisions that quantifies the elasticity of particle collisions. (g_0) is the radial distribution function that can also be seen as a probability for interaction between particles. Different models exists, they are formulated is in table 2. The solid bulk viscosity λ_S accounts for the granular particles resistance of compression and expansion. It can be calculated by the following form

(Ekambara et al. [2009]):

$$\lambda_S = \frac{4}{3}\alpha_S \varrho_S d_S g_0 \left(1+e\right)\left(\frac{\Theta_S}{\pi}\right)^{\frac{1}{2}} \tag{3.8}$$

Then, the solid shear viscosity μ_S based on granular kinetic theory consists of a collisional contribution and from a kinetic contribution. It can be represented as (Gidaspow [1994]):

$$\mu_S = \mu_{S,\text{col}} + \mu_{S,\text{kin}} \tag{3.9}$$

Table 2 show different Kinetic Theory Correlations for μ_S and g_0.

Table 3.1: Kinetic Theory Correlations

	Granular viscosity μ_s
Lun et al. [1984]	$\frac{4}{5}\alpha_s^2\varrho_s d_s g_0(1+e)\sqrt{\frac{\Theta}{\pi}} + \frac{1}{15}\sqrt{\Theta\pi}\frac{\varrho_s d_s g_0(1+e)\left(\frac{3}{2}e-\frac{1}{2}\right)\alpha_s^2}{\frac{3}{2}-\frac{1}{2}e} + \frac{1}{6}\sqrt{\Theta\pi}\frac{\varrho_s d_s \alpha_s\left(\frac{s}{2}e+\frac{1}{4}\right)}{\frac{3}{2}-\frac{e}{2}} + \frac{10}{96}\sqrt{\Theta\pi}\frac{\varrho_s d_s}{(1+e)\left(\frac{3}{2}-\frac{1}{2}e\right)g_0}$
Syamlal et al. [1993]	$\frac{4}{5}\alpha_s^2\varrho_s d_s g_0(1+e)\sqrt{\frac{\Theta}{\pi}} + \frac{1}{15}\sqrt{\Theta\pi}\varrho_s d_s g_0\frac{(1+e)\left(\frac{3}{2}e-\frac{1}{2}\right)}{\frac{3}{2}-\frac{e}{2}}\alpha_s^2 + \frac{1}{12}\frac{\alpha_s d_s \varrho_s\sqrt{\pi\Theta}}{\frac{3}{2}-\frac{e}{2}}$
Gidaspow [1994]	$\frac{4}{5}\alpha_s^2\varrho_s d_s g_0(1+e)\sqrt{\frac{\Theta}{\pi}} + \frac{1}{15}\sqrt{\Theta\pi}\varrho_s d_s g_0(1+e)\alpha_s^2 + \frac{1}{6}\sqrt{\Theta\pi}\varrho_s d_s \alpha_s + \frac{10}{96}\sqrt{\Theta\pi}\frac{\varrho_s d_s}{(1+e)g_0}$
Hrenya and Sinclair [1997]	$\frac{4}{5}\epsilon_s^2\varrho_s d_s g_0(1+e)\sqrt{\frac{\Theta}{\pi}} + \frac{1}{15}\sqrt{\Theta\pi}\frac{\varrho_s d_s g_0(1+e)\left(\frac{3}{2}e-\frac{1}{2}\right)\epsilon_s^2}{\left(\frac{3}{2}-\frac{c}{2}\right)} + \frac{1}{6}\sqrt{\Theta\pi}\frac{\varrho_s d_s \epsilon_s\left(\frac{1}{2}\left(1+\frac{\lambda_m f_p}{R}\right)+\frac{3}{4}e-\frac{1}{4}\right)}{\left(\frac{3}{2}-\frac{1}{2}e\right)\left(1+\frac{\lambda_m(p)}{R}\right)} + \frac{10}{96}\sqrt{\Theta\pi}\frac{\varrho_s d_s}{(1+e)\left(\frac{3}{2}-\frac{1}{2}e\right)g_0\left(1+\frac{\lambda_m f_p}{R}\right)}$
	Radial Function g_0
Carnahan and Starling [1969]	$\frac{1}{1-\epsilon_s} + \frac{3\epsilon_s}{2\left(1-\epsilon_s\right)^2} + \frac{\epsilon_s^2}{2\left(1-\epsilon_s\right)^3}$
Lun and Savage [1986]	$\left(1-\frac{\alpha_s}{\alpha_{s,\max}}\right)^{-2.65\alpha_{s,\max}}$
Sinclair and Jackson [1989]	$\left[1-\left(\frac{\alpha_s}{\alpha_{s,\max}}\right)^{\frac{1}{3}}\right]^{-1}$
Gidaspow [1994]	$\frac{3}{5}\left[1-\left(\frac{\alpha_s}{\alpha_{s,\max}}\right)^{\frac{1}{3}}\right]^{-1}$

Remarks:

For granular viscosity:

- Hrenya and Sinclair [1997] follow Lun et al. [1984] but constrain the mean free path of the particle by a dimension characteristic of the actual physical system. This is opposed to the Lun et al. [1984] theory which allows the mean free path to tend toward infinity.
- Lun et al. [1984] theory which allows the mean free path to tend toward infinity and the solids viscosities tends toward a finite value as the solids volume fraction tends to zero.
- By constraining the mean free path, the limit of the Hrenya and Sinclair [1997] shear viscosity expression correctly tends to zero as the solids volume fraction approaches zero.
- Syamlal et al. [1993] solids shear viscosity also tends to zero as the solids volume fraction tends to zero. In this case, however, the solids shear viscosity limit is reached because the kinetic contribution to the solids viscosity is neglected.

For radial function:

- The Carnahan and Starling [1969] expression, however, does not tend toward the correct limit at closest solids packing. Because particles are in constant contact at the maximum solid volume fraction, the radial distribution function at contact tends to infinity.
- Alternate expressions to the Carnahan and Starling [1969] expression have been proposed by Gidaspow [1994], Lun and Savage [1986] and Sinclair and Jackson [1989] which tend to the correct limit at closest packing.

The KTGF models are choosed based on a sensitivity analysis where the Syamlal et al. [1993] model for the granular viscosity gave better results and were more stable, along with Sinclair and Jackson [1989] model for the radial function.

When the solid phase fraction is high in a particular zone of the domain, lots of contacts among particles occur and a frictional stress derives from them that must be accounted for in the mathematical model. In this state the collisions among particles could not

be considered instantaneous as previously done in the kinetic theory and the frictional stress is accounted for adding a term in the granular pressure and in the granular viscosity. Hence, the solid shear viscosity μ_S is expressed by Eq.(3.10):

$$\begin{aligned} \mathcal{P}_{\mathfrak{s}} &= \mathcal{P}_{\text{kinetic}} + \mathcal{P}_{\mathfrak{s},\mathfrak{fr}} \\ \mu_{\mathfrak{s}} &= \mu_{\text{kinetic}} + \mu_{\mathfrak{s},\mathfrak{fr}} \end{aligned} \tag{3.10}$$

$$\mathcal{P}_{\mathfrak{s},\mathfrak{fr}} = \mathcal{F}\mathfrak{r}\frac{(\alpha_{\mathfrak{s}} - \min(\alpha_{\mathfrak{s}}))^{\mathfrak{n}}}{(\alpha_{\mathfrak{s},\max} - \alpha_{\mathfrak{s}})^{\mathfrak{p}}} \tag{3.11}$$

where $\mathcal{F}\mathfrak{r} = 0.05$, $\mathfrak{n} = 2$ and $\mathfrak{p} = 5$ are empirical constants. The frictional shear viscosity is than expressed by:

$$\mu_{\mathfrak{s},\mathfrak{fr}} = \mathcal{P}_{\mathfrak{s},\mathfrak{fr}} \sin\delta \tag{3.12}$$

being δ the angle of internal friction of the particle. **NB**: The frictional stress is added to the stress predicted by the kinetic theory when the solids volume fraction exceeds a critical value. This value is normally set to 0.5 when the flow is three-dimensional and the maximum packing limit is about 0.63.

3.2 Pressure drop calculations

The single-phase flow simulations are carried out to validate the modeling approach, the choice of the turbulence model as well as various essential parameters in order to carry out the treatment of the area near the wall. Also to validate the surrogates models construction approach. The pressure drop data for different water flow rates is recorded for cases of : horizontal pipe, inclined pipe and pipe with elbow. The results of the CFD code are compared with predicted values from theoretical correlations found in the literature. Table 3.2 shows different correlations to calculate the pressure drop for each setup. The implicit relation proposed by Colebrook, Eq.(3.13), is used to calculate the friction factor for turbulent flows in rough pipes.

$$\frac{1}{\sqrt{f}} = -2\log\left(\frac{e}{3.71D} + \frac{2.51}{\text{Re}\sqrt{f}}\right) \tag{3.13}$$

Table 3.2: Pressure drop correlations

Correlations	Pipe Set up
$\Delta\mathcal{P}_{\mathfrak{f}} = -\mathfrak{f}\frac{\varrho_{\mathfrak{W}}\mathrm{L}}{\mathrm{D}}\frac{\mathrm{U}_{\mathfrak{W}}{}^{2}}{2}$	Horizontal Pipe
$\Delta\mathcal{P} = -\Delta\mathcal{P}_{\mathfrak{f}} - \varrho_{\mathfrak{W}}\mathfrak{g}\mathfrak{L}\mathfrak{sin}(\theta)$	Inclined Pipe
$\Delta\mathcal{P} = -\Delta\mathcal{P}_{\mathfrak{f}} - \varrho_{\mathfrak{W}}\mathfrak{g}\mathfrak{L}_{\mathfrak{inclined}}\mathfrak{sin}(\theta) - \mathcal{K}_{\mathfrak{L}}\frac{\varrho\mathcal{U}_{\mathfrak{W}}^{2}}{2}$	Pipe with Bend

where $\frac{e}{D}$ is the relative roughness, and is related the pipe material properties.

3.3 Turbulence model

The turbulence aspect must be ensured when transporting a slurry. Since, this will guarantee the pseudo-homogeneity of the mixture and will subsequently prevent total sedimentation of the solid phase. In this work, the flow is characterized by a Reynolds number of order of 10^6. This is why the turbulence of water for both single or two phase flow is treated with the standard k- ϵ model, which is a high Reynolds turbulence model. However, wall functions are used to treat the boundary-layer development up to the wall. Eq.(3.14) and Eq.(3.15) present the model variables, the turbulent kinetic energy k and the turbulence dissipation rate ϵ respectively:

$$\frac{\partial(\varrho_W k_W)}{\partial t} + \frac{\partial\left(\varrho_W k_W U_{W_i}\right)}{\partial x_i} = \frac{\partial}{\partial x_j}\left[\left(\mu_W + \frac{\mu_t}{\sigma_k}\right)\frac{\partial k_W}{\partial x_j}\right] + G_k + G_b - \varrho_W \varepsilon_W + S_k \quad (3.14)$$

$$\frac{\partial(\varrho_W \varepsilon_W)}{\partial t} + \frac{\partial\left(\varrho_W \varepsilon_W U_{W_i}\right)}{\partial x_i} = \frac{\partial}{\partial x_j}\left[\left(\mu + \frac{\mu_t}{\sigma_\varepsilon}\right)\frac{\partial \varepsilon_W}{\partial x_j}\right] + \frac{C_{1\varepsilon}\varepsilon_W}{k_W}\left(G_k + C_{3\varepsilon}G_b\right) - C_{2\varepsilon}\varrho\frac{\varepsilon_W^2}{k_W} + S_\varepsilon \quad (3.15)$$

3.4 Near-wall treatment

The near-wall treatment is done using the wall functions method. The wall functions consist of wall boundary conditions that impose values for the kinetic energy k_P and the dissipation rate ϵ_P in the center of the cells near the wall as shown by Eq.(3.16) and Eq.(3.17), which bridges turbulent quantities on the wall.

$$k_P = \frac{\sqrt{f U_W^2}}{\sqrt{2C\mu}} \tag{3.16}$$

$$\epsilon_P = \frac{C_\mu^{3/4}\ K_P^{3/2}}{k\ y_P} \tag{3.17}$$

$C_\mu = 0.09$ is a model coefficient of the $k - \epsilon$; $k = 0.41$ is Von Karman constant; y_P is the height to the center of the cell adjacent to the wall and it can be calculated from y^+ according to the Eq.(3.18).

$$y_p = \frac{y^+ \mu_W}{\varrho_W \sqrt{f u_W}} \tag{3.18}$$

For the inlet turbulence conditions, Eq.(3.19) present the turbulent kinetic energy (k_{in}) that is obtained from the turbulence intensity (I) and the water inlet velocity (U_W) (Messa and Matoušek [2020]):

$$k_{in} = \frac{3}{2} U_W^2 I^2 \tag{3.19}$$

Next, the length scale (l) of the turbulence at the inlet should be specified. For an internal pipe flow, this is usually $\sim 7\%$ of the pipe diameter. So the turbulent dissipation rate (ϵ_{in}) is calculated as shown in Eq.(3.20):

$$\epsilon_{in} = C_\mu \frac{k_{in}^{3/2}}{l} \tag{3.20}$$

3.5 Methodology

After choosing the mathematical models necessary to simulate the diphasic flow, comes the part of the implementation under the CFD tool. In this work the open-source CFD

toolbox Open∇FOAM® was choosed to perform the simulations, considering its advantages by comparing it with other CFD tools. Table 3.3 shows Open∇FOAM® software advantages compared to commercial softwares..

	Open∇FOAM®	commercial Softwares
Cost effectiveness	✓	✗
Parallel computing	✓	✓
Source code	✓	✗
Redistribution of code	✓	✗
Collaboration development	✓	✗
Documentation	✗	✓
GUI / user friendlness	✗	✓

Table 3.3: Comparison between Open∇FOAM® and commercial software like ANSYS, STAR-CCM+, etc

The simulation workflow begins with the pre-processing where the geometry along with the mesh are generated, after comes the part of choosing the solver which represent well our model, and then the post-processing where the results of the simulation are visualized. The twoPhaseEulerFoam solver is the one which represents well our model and the solver has been modified to become an isothermal flows solver, since there is no heat exchange between the phases. Then, in the constant file the different forces which act on the flow have been defined according to the assumptions made, where thus the interphase momentum exchange models have been defined. Then the components of the KTGF are implemented taking into consideration the restitution coefficients. The implementation of the model also requires special attention to the boundary conditions which need a good understanding of the physical phenomenon to define them.

Chapter 4

Results and discussions

4.1 Single phase flow

To carry out validation of the mathematical model along with the turbulence model and the treatment process for the area near the wall, simulations for a single phase flow are performed for three pipe setups. Moreover, these simulations will help to validate the approach of constructing surrogates models. The predicted values of the theoretical correlations presented in section 3.2, are used to judge the CFD results. The implementation of the models is done under the OpenFOAM software V7. Table 4.1 summarizes different boundary conditions for different inputs.

Table 4.1: Summary of the selected boundary conditions

Field	Inlet	Outlet	Solid walls
ϵ_W	fixedValue	zeroGradient	wall function
k_W	fixedValue	zeroGradient	wall function
v_t	zeroGradient	zeroGradient	wallFunction
p	zeroGradient	atmospheric pressure	zeroGradient
U_W	fixedValue	zeroGradient	noSlip

Horizontal pipe

The geometry consists of a 40 m horizontal pipe, with an internal diameter of 0.9 m. Figure 4.1(a) and 4.1(b), shows a 2D section and the 3D meshed geometry. GMSH software was used to generate a specific mesh which takes into account the near-wall refinement by calculating the height of the first cell on the wall, with a precise magnification ratio which is linked to y^+ while approaching the center of the pipe. The flow consists of water with a density $\varrho = 1000 kg/m^3$. The Wall roughness is set at 0.045 mm. The inlet velocity is in ranges of 1 to 3 m/s. The pressure at the outlet is fixed as atmospheric pressure. The latter initial condition is the same for the next simulations of inclined and bended pipe.

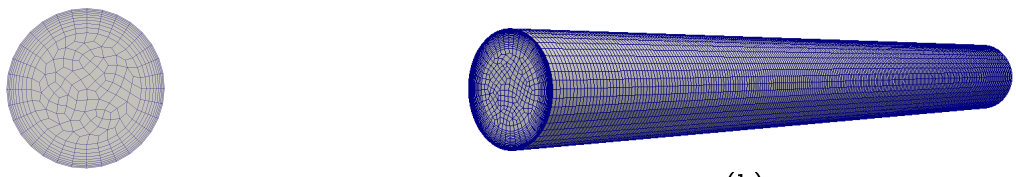

(a) (b)

Figure 4.1: Horizontal pipe geometry: (a) Cross-section mesh, (b) Profile mesh

For a horizontal pipe, we have regular pressure drops, which are generated by the friction of the fluid on the internal wall of the pipe throughout its passage. They depend on, the length of the pipe, the relative roughness of the pipe, the speed of the fluid circulating in the pipe (U_{in} m/s), as presented in table 1. Therefore, As can be seen in Figure 4.2, the pressure losses are increasing relatively with inlet velocities. For this current case of a horizontal pipe, experimental data were found for water flow in (Gillies et al. [2004]), and also a good agreement was found with cfd results as shown in Figure 4.2.

The mean average percentage error is defined as follows:

$$\text{MAPE} = \left\{ \frac{1}{n} \sum_{k=1}^{n} \left[\frac{(dp/dx)_{\text{pred}} - (dp/dx)_{\text{theory}}}{(dp/dx)_{\text{theory}}} \right] \right\} 100 = 1.21\%$$

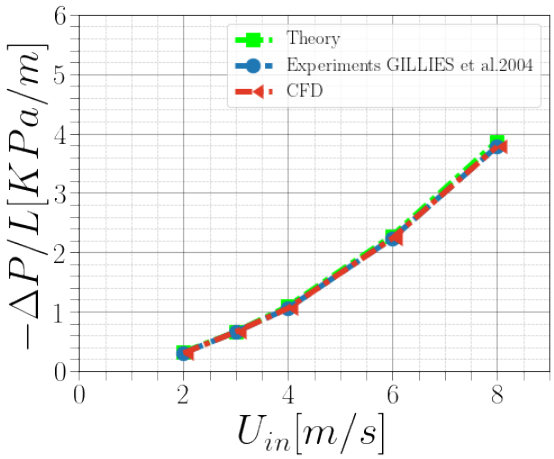

Figure 4.2: Pressure drop in horizontal pipe. Present pressure drops from CFD simulations versus empirical formula in table 3.2 and experimental measurements.

Inclined pipe

In this section, the geometry consists of a 40 m inclined pipe with 0.9 m diameter and a 5.73 degree negative slope. Figure 4.3(a) and 4.3(b) show the cross-section and profile mesh.

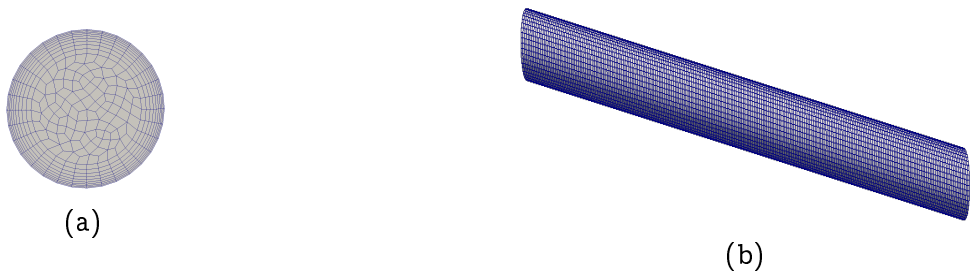

Figure 4.3: Inclined pipe geometry: (a) Cross-section mesh, (b) Profile mesh

Concerning this pipe setup, it is characterized by a changing elevation. Consequently, at the end of the inclined pipe there is the full weight of fluid pushing down on that point and due to this, the pressure at that point increases. Therefore, there is a pressure gain in the pipe as the fluid goes down. The total pressure difference can be calculated by adding the hydrostatic pressure to the friction component as in table 3.2. Figure 4.4, show the pressure gradient as a function of inlet velocities. As noticed the pressure gain decreases while increasing the velocity, and this comes back to the augmentation of friction losses. The mean average percentage error $(MAPE) = 0.97\%$

Bended pipe

For this setup, the geometry consists of a 45 degree bended pipe, of 6 m equivalent length with 0.9 m diameter. Figure 4.5(a) and 4.5(b) show the cross-section and profile mesh.

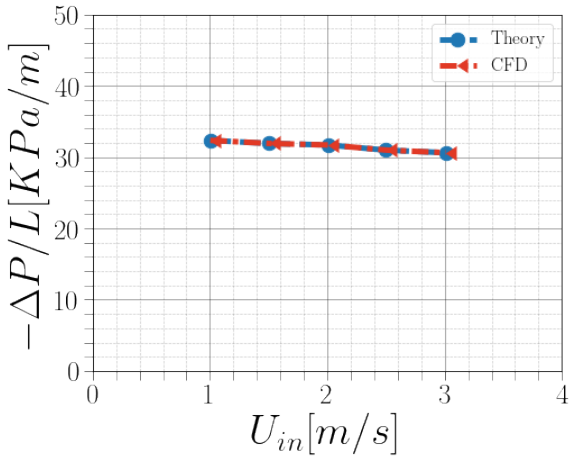

Figure 4.4: Pressure drop in inclined pipe

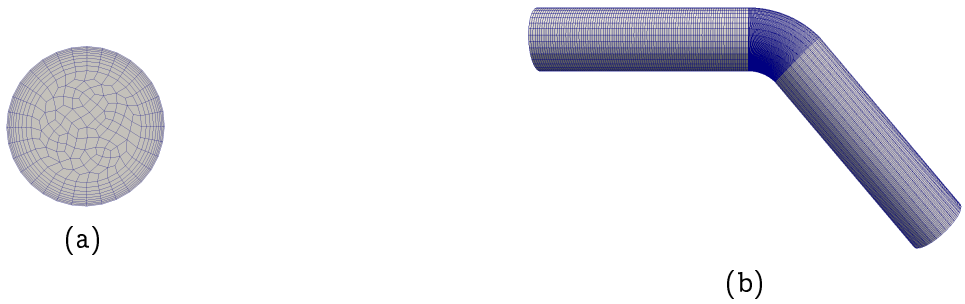

Figure 4.5: Bended pipe geometry: (a) Cross-section mesh, (b) Profile mesh

This pipe setup is more complex, since in addition to the previously discussed components of the kinetic losses, another component is added namely the singular pressure drop as in table 3.2. The singular pressure drops are mainly due to the geometric modification of the pipe, such as changes of direction like bends. Figure 4.6 shows that the pressure loss is increased in such geometries. The mean average percentage error $(MAPE) = 7.99\%$

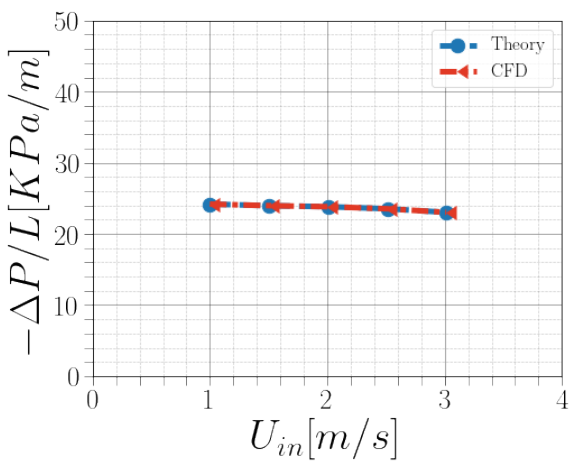

Figure 4.6: Pressure drop in bended pipe. The empirical formula slightly underestimates the pressure drop versus the CFD simulations

The pressure drop formulae constitute surrogate models for pressures calculations in piping systems with newtonian fluids such as water. From the previous analysis we see that CFD reproduces very well the pressure drop measurement and the empirical models fits the CFD results for the classical geometrical configurations. Hence, one can consider for example computing other pressure drop models for Newtonien fluids but for much more complex geometries, where experiments may be complex or time consuming to conduct. In the next section we will consider a different case, where the complexity is introduced in the fluid itself. And the aim is to use the CFD approach to develop pressure drop models for complex fluids. Morevoer, once the simulations validated they can be used to develop response models (or surrogate models) for other physical quantities than pressure drops. For instance, in a slurry pipe flow a sedimentation model along pipe of different geometries can be usefull for applications.

4.2 Two phase flow

An attempt to simulate the behaviour of a sediment-water mixture during its transportation through a pipe has been made, using the twoPhaseEulerFoam solver available in the 6.0 release of the open-source CFD toolbox Open∇FOAM®. The geometry used consisted of a pipe of length L = 0.02 m, a diameter D = 0.0001 m. The flow is laminar with Re = 144, , $\varrho_S = 1,450 kg/m^3$, $\varrho_W = 1,027 kg/m^3$, $V_{mixture} = 1 m/s$, $d_S = 70\mu m$, $\mu_W = 0.00891 kg/m.s$, $\alpha_{0S} = 30\%$, $P_0 = 10^5 Pa$. Figure 6 and 7, show the 2D and 3D meshed geometry. OpenFOAM's meshing utility blockMesh was used to generate structured orthogonal meshes about 200 cells along the pipe.

- **Pre-processing: 2D and 3D meshed geometry**

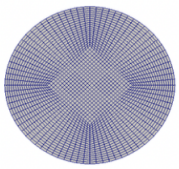

(a) Cross-section mesh

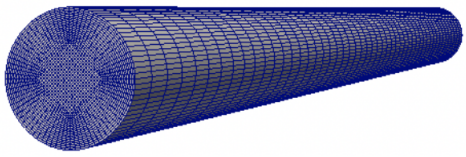

(b) 3D pipe mesh

- **Post-processing**

Figure 4.8(a) and 4.8(b) show the solid concentration for the cross-section of the pipe and along the pipe respectively. These first results show an agreement with one of the types of two-phase flows found in the literature, which is a sliding bed flow. While, 4.8(c) shows that the condition of the fractional volumes sum for the two phases is equal to 1, throughout the diameter in the pipe outlet.

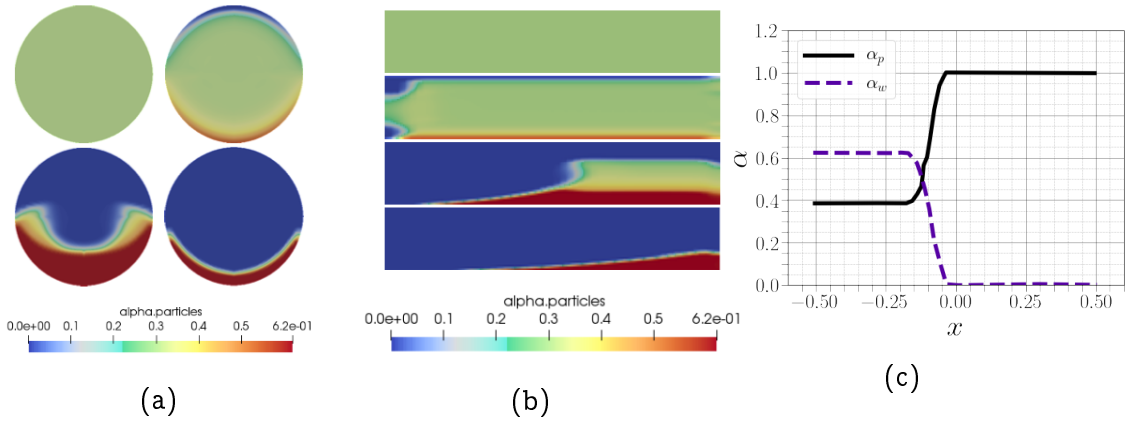

Figure 4.8: Bended pipe geometry: (a) Cross-section Concentration at the outlet, (b) Concentration along the pipe, (c) Volume fraction of both phases

Two phase simulations were presented by authors in (Elkarii et al. [2020]), where a slurry of mono-dispersed spherical polystyrene beads with rhodorsil silicone oil were simulated in a laminar flow. Figure 4.9 shows the evolution of the solid concentration profile of the mixture over time.

The previous study (Elkarii et al. [2020]), validates the model for its capability to reproduce and predict high volume concentration profiles up to 60 %. The validation case consists of a sedimentation of non-cohesive particles by Chauchat et al. [2017], based on experimental data from (Pham Van Bang et al. [2008]). The sedimentary phase was also modeled as continuous and consecutive laws were adopted to take sedimentary constraints into account. However, to approach the simulation of a real slurry flow, the turbulence aspect must be added to prevent sedimentation problems. Therefore, in this part, CFD simulations were performed to fit the experimental results of a turbulent flow of water-sand slurry under isothermal conditions, reported by Gillies et al. [2004]. Experimental data consists of pressure drops along the pipe, particle concentration profiles and particles velocity profiles at the pipe outlet. The simulation domain consists of a 10 m long pipe. boundary conditions set are the inlet, the outlet and the lateral surface which is referenced as walls, are presented in the table 4.2. The mass flow rates of the two phases, $\dot{m}_W$ and $\dot{m}_S$ are fixed at the inlet boundary, and calculated as in Eq.(4.1), the turbulent kinetic energy of the liquid, k_{in}, and its dissipation rate, ϵ_{in}, were also fixed as in Eq.(3.19) and Eq.(3.20).

$$\dot{m}_W = \alpha_W \varrho_W U_W A; \quad \dot{m}_S = \alpha_S \varrho_S U_S A \tag{4.1}$$

The numerical simulations performed in this section, uses the same mesh configuration, as in section 4.1, except that the meshes have been refined in all directions. The flow is characterized by high inlet velocities ranging up to 8 m/s. Two diameters of particles are considered, along with different

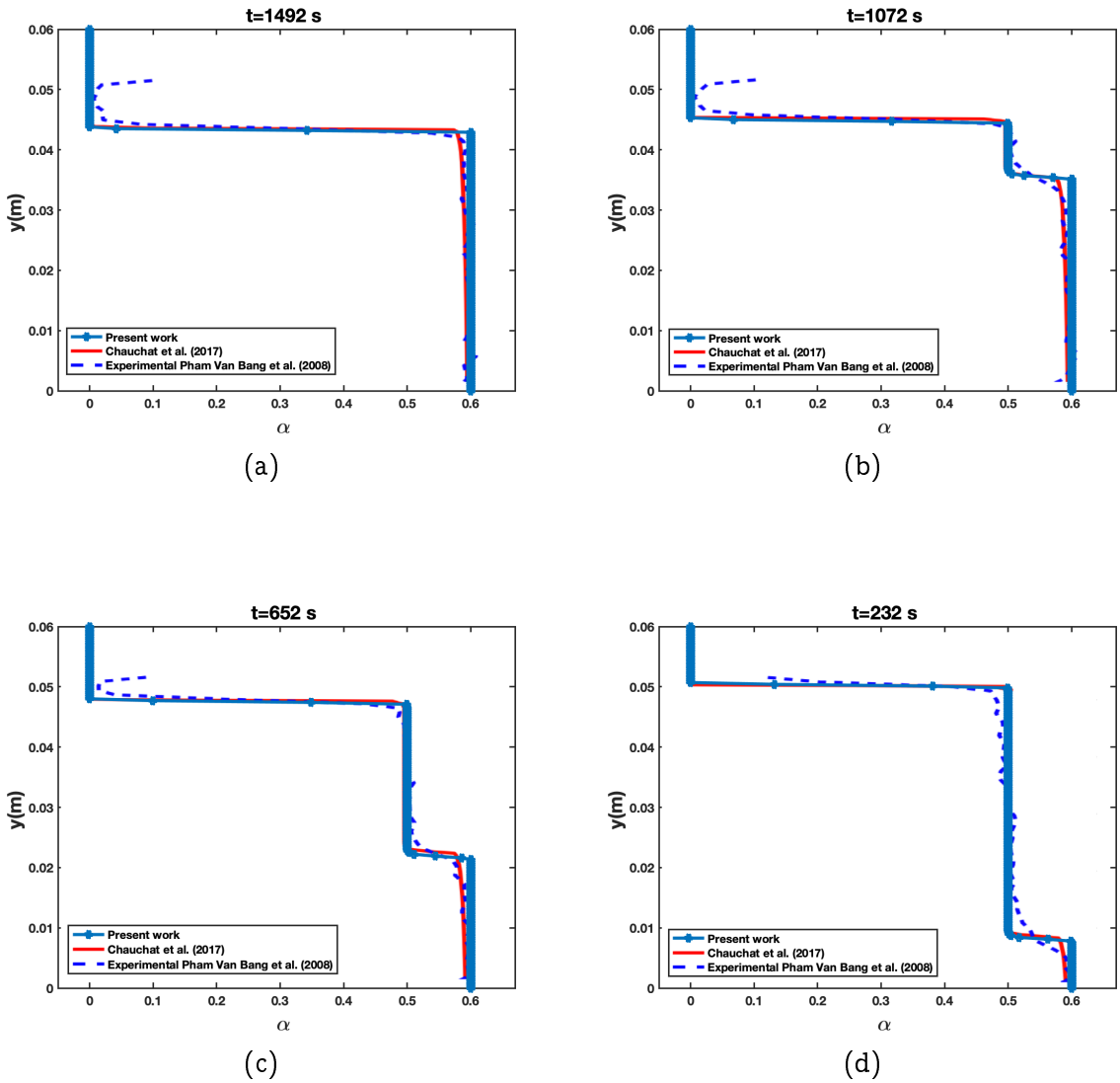

Figure 4.9: Sediment concentration profiles over time (a) At t = 232 s, (b) t = 652 s (c) t = 1072 s (d) t = 1492 s

Table 4.2: Summary of the selected boundary conditions

Field	Inlet	Outlet	Solid walls
α_s	fixedValue	zeroGradient	zeroGradient
α_W	fixedValue	zeroGradient	zeroGradient
ϵ_W	fixedValue	zeroGradient	wall function
k_W	fixedValue	zeroGradient	wall function
v_t	zeroGradient	zeroGradient	wall function
p	fixedFluxPressure	atmospheric pressure	zeroGradient
θ_p	fixedValue	zeroGradient	JohnsonJacksonParticleTheta
U_W	mass flow rate	zeroGradient	noSlip
U_S	mass flow rate	zeroGradient	JohnsonJacksonParticleSlip

solid concentrations. The physical parameters used are sand density $\varrho_s = 2650\ kg/m^3$, water density $\varrho_W = 1000\ kg/m^3$, and water viscosity $\mu_w = 10^{-3} kg/m.s$. The radial distributions of sand particles for two inlet concentrations are presented in figure 4.10. Regarding the experimental results, the solid concentration profile varies slightly along the diameter of the pipe ($0.19 < \alpha_s < 0.24$). The present simulation in figure 4.10(a) agrees fairly well with the experiments in the bulk flow ($0.2 < r/D < 0.9$), whereas the model underestimate the experimental values of α_s near the upper wall ($r/D > 0.9$), and on the other hand, overestimate them along the lower wall ($r/D < 0.2$). In the present model, it can be attributed to the none total control of the turbulent viscosity term, which promotes the phenomenon of sedimentation, resulting in a non-homogeneous concentration profile. On figure 4.10(b) the solid concentration is increased up to 33 %, but, the same behavior is always observed, and corresponds to a pseudo-homogeneous flow with formation of a small bed of particles.

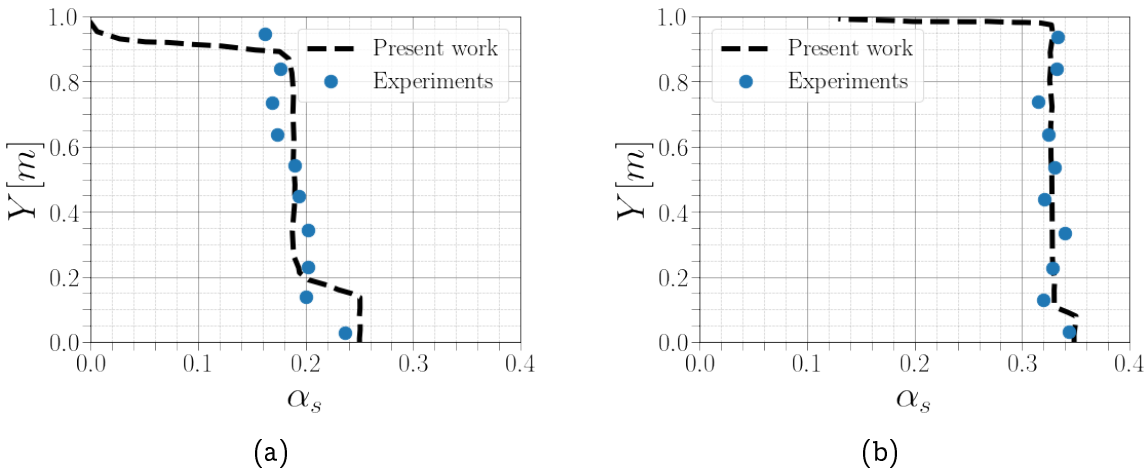

Figure 4.10: Radial distributions of the volume fraction of sand particles of $d_p = 0.09mm$ for $U_{in} = 3m/s$: (a) ($\alpha_{s,in} = 0.19$), (b) ($\alpha_{s,in} = 0.33$)

The particles velocity profiles for $U_{in} = 2m/s$ and $U_{in} = 3m/s$ are presented in figure 4.11(a) and 4.11(b) respectively. On the contrary to the concentration distribution, the present model predicts the right profile of velocity. It is remarked that the axial average velocities distributions are symmetrical, and they agree almost exactly to a classic turbulent parabolic profile. This comes down to the fact that the presence of particles does not greatly influence the current field. This is explained by the constant solid concentration around the value 0.2 for the entire pipe and the dynamic viscosity of the fluid then varies slightly .

Figure 4.12 (a) and (b) shows the variations of the pressure drop per unit length $\Delta P/L$ with the inlet velocity of the mixture U_{in}. The present simulations obtained for two different particles diameters $d = 0.09mm$ and $d = 0.27mm$, for nearly the same inlet concentration, and for a high velocities.

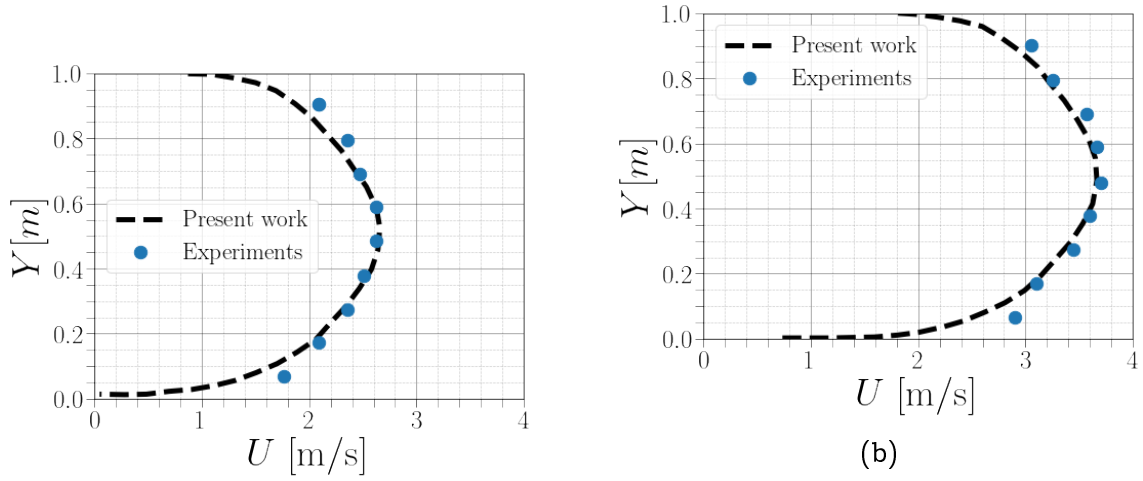

(a) (b)

Figure 4.11: Radial distributions of the mean axial velocity of sand particles at the outlet of the pipe, for $\alpha_s in = 0.19$ and $d_p = 0.09mm$: (a) ($Uin = 2m/s$), (b) ($Uin = 3m/s$).

Experimental data from (Gillies et al. [2004]) is used as a validation for current simulations. The pressure drop analyzed in current simulations augments almost linearly with U_{in}. As anticipated, the pressure drop increases because of the increased values of friction losses. Results fit well in figure 4.12 (a) for $d = 0.09mm$, However, discrepancies are higher at high velocities. Contrary to figure 4.12 (b) for $d = 0.27mm$, a very good agreement is observed at high velocities, and a large gap is visible at low input velocities $U_{in} \leq 3m/s$.

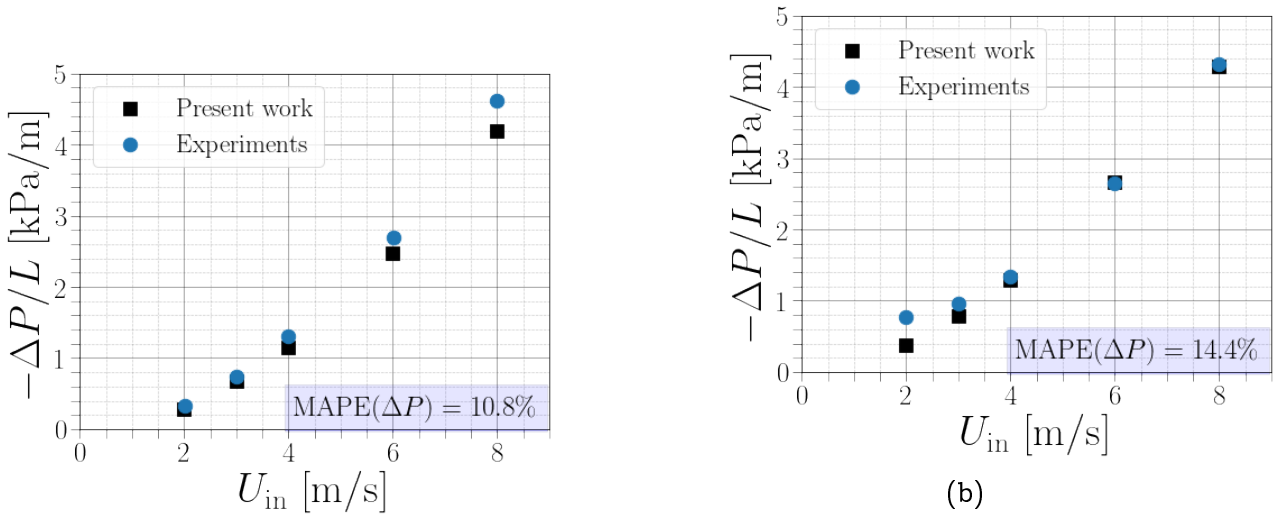

(a) (b)

Figure 4.12: Pressure drop per unit of length $\Delta P/L$ versus slurry velocity: (a) ($\alpha_S = 0.19$, $d = 0.09mm$), (b) ($\alpha_S = 0.20$, $d = 0.27mm$).

It is also noted, that coarser particles compared to smaller ones, have superior pressure drop at lower flow rates and have an inferior one at higher flow rates. The reason behind this, is that the coarser particles at lower speeds deposit more which comes down to the gravitational effect, and subsequently, the amount of particles in the bed increases which leads to more frictions. While, in the case of smaller particles at higher velocities, the pressure losses are bigger due to the larger surface area of the material.

4.3 Surrogate model

Once the CFD results are validated with experimental data, this work aims to construct a surrogate model for the pressure drops for a two-phase flow within a piping system. The proposed model uses the empirical formula in Table 3.2 for the pressure losses due to frictions for horizontal pipes. The density, however, is that of the water-sand mixture. The model has been calibrated to find the optimal friction factor f, that fit well with the CFD results trough a minimization process (figure 4.13), for different solid concentration α_s and two particle sizes d_p. So that the calculations of the pressure drops by the empirical formula correspond well to the CFD results. Figure 4.14 shows the variation of the calibrated

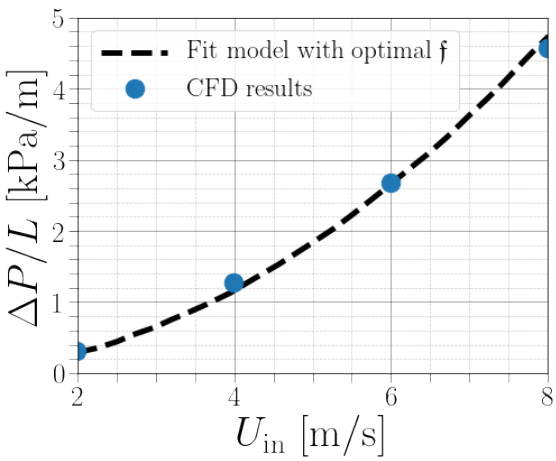

Figure 4.13: Example of fitting of the empirical formula of pressure drop with the CFD results for $\alpha_S = 0.19$ and $d_p = 0.09mm$.

friction factor $f(\alpha_s, d_p)$ as function of the solid volume concentration for two different particle sizes. According to figure 4.14, one can for example for a given α_S and the specified particle diameters, interpolate to find values of f and then predict the pressure drop by substituting the found value of f in the empirical formula.

Generalized Polynomial Chaos (gPC)

With the growing computational techniques, numerical simulators have been frequently employed to predict the behavior of physical systems. Uncertainties are inevitable in the implementation of system

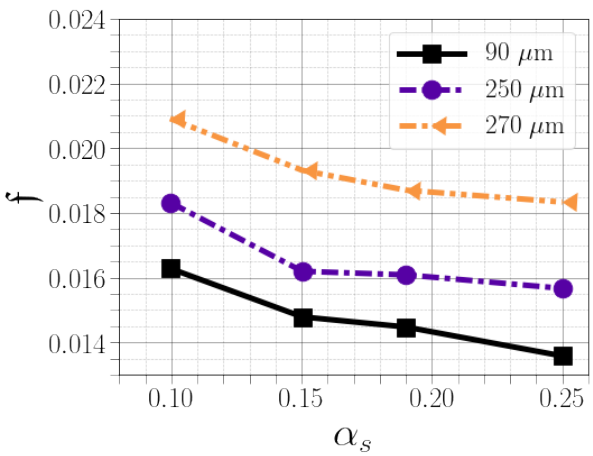

Figure 4.14: Optimal calibrated values of the friction factor along with the variation of the solid concentration for particles with diameter $d_p = 0.09$ and $d_p = 0.27$.

models when coping with real-world problems. In CFD applications, numerical models are built to simulate complex fluid flows around rigid or flexible profiles. They are implemented in computer programs which tend to become more and more sophisticated and extensive. These models often exhibit certain features that may be considered as uncertain, or they depend on parameters that may be considered as such. Propagation and quantification of uncertainty aim at establishing a quantitative assessment of and some insight into the impact that these uncertainties have on the predictions given by the models. Statements about the influence of uncertainties may serve to guide the allocation of resources in order to reduce them, but are also essential in the process of validating the models in the presence of uncertain parameters or in the process of optimizing. Monte Carlo (MC) simulation is by far the most popular method for uncertainty quantification (UQ). It evaluates the system model at a large number of input samples and analyzes the statistical quantities of interest (such as mean and variance) from the sampling results Doucet et al. [2001]. For those CPU-demanding models, it may pose a prohibitively large computational cost. As an efficient alternative, the polynomial chaos expansion (PCE) method employs a set of orthogonal polynomials as the basis functions to approximate the model responses Ghanem and Spanos [2003], the statistical quantities of interest can then be calculated directly from the expansion coefficients according to the orthogonality property. The Polynomial Chaos (PC) expansion [Najm [2009], DeGennaro et al. [2015]] has probably become the most widely used meta-model for propagating uncertainties. PC was originally proposed by Wiener [1938], under the name of Homogeneous Chaos, to model stochastic response resulting from a stochastic process with normally distributed random variables using Hermite polynomials. Only years later, Xiu and Karniadakis [Xiu and Karniadakis [2002], Xiu and Karniadakis [2003]] generalized the method to other types of statistical distributions (uniform, beta, gamma...) and showed that the relative error in the statistical moments decreases exponentially when the Askey scheme is used Askey and Wilson [1985]. The method is now better known as generalized PC (gPC). The gPC, offers a large potential for computational fluid dynamics (CFD) related

non-deterministic simulations, as it allows the treatment of a large variety of stochastic variables and properties that can be described by probability density functions (PDFs). The stochastic solution is expanded into series of orthogonal polynomials in the space of those random variables. Those orthogonal polynomials are chosen in accordance with the probability density function of the input parameters following the so-called Askey scheme of polynomials. The gPC can be implemented either in an intrusive or in a non-intrusive way as follows.

Intrusive Polynomial Chaos

The intrusive PC expansion originally introduced in [Ghanem and Spanos [2003], Jahedi and Ahmadi [1983], Sun [1979]] is based on a Galerkin-type projection formulation of the model equations, Dinescu et al. [2010] showed the first application of intrusive PC to the 3D Navier-Stokes equations. It consists in introducing the calculation of the coefficients of the PC directly into the numerical model. For each unknown u is therefore replaced with its expansion coefficients u_i. The number of unknowns is therefore basically multiplied with a factor $P + 1$, which can be quite high for high stochastic dimensions and/or high polynomial order. This approach is very delicate to implement and poses difficulties for strongly nonlinear models Berveiller [2005]. It requires important changes to the CFD code, making it less attractive for industry who are relying on their own well validated codes, or for use with commercial softwares. As a result attention was focused on non-intrusive approaches requiring no change in the CFD code. When it comes to consider variable parameters for sensitivity and robustness analyses, non-intrusive methods for uncertainty quantification (UQ) are typically considered in CFD.

Non-Intrusive Polynomial Chaos

Regarding non-intrusive PC expansions, it does not require modifying the numerical model but considers it as a black box. The PC coefficients are determined after evaluating the numerical model at different points in the parameter space, which requires a design of experiments. Two approaches for computing the PC coefficients of the output quantities of interest have usually been considered: (i) the projection approach, in which they are computed by structured quadratures, i.e., Gauss quadratures, or unstructured quadratures, i.e., Monte Carlo or quasi Monte Carlo sampling; and (ii) the regression approach, minimizing some error measure or truncation tolerance of the PC expansion for some particular values of the inputs. In both cases, a series of deterministic simulations for different realizations of the uncertain parameters must be calculated. Practical application of these techniques to CFD problems is available in [Reagana et al. [2003], Berveiller et al. [2006]]. A major drawback is that the number of model evaluations grows exponentially with both the number of uncertainties and the PC expansion order. In the literature, this drastic increase in computational cost with the number of random variables is often referred to as the curse of dimensionality. This issue seriously restricts the practical use of PC in industrial applications, which are inherently characterized by a large number of uncertainties. Therefore, an efficient UQ scheme must be defined to overcome this issue. Fortunately, the Smolyak algorithm

Smolyak [1963] defines sparse grid quadratures involving less points while preserving a satisfactory level of accuracy.

Chapter 5

Conclusion

This paper is about modelling slurry flows in pipelines. A quite vast review of the literature of previous CFD investigations on slurry flow in horizontal pipelines was realized first, to decide on the relevant modeling approaches as well as the corresponding mathematical models. Based on this state of art, the two fluid model was the one chosen to work with, because it has the ability to capture well the physics of such complex flows while ensuring moderate computing time. Then, it was decided to begin with simulations of single phase flow into different pipe setups, to validate the turbulence model and to validate the approach of constructing a surrogate model throughout 3D numerical simulations. In this part CFD results matches the empirical data and theoretical models for pressure loss, also a really good agreement versus experimental data even at high velocities was found. After that, two phase flow simulations are performed, to investigate the physical phenomenons within such flows. CFD results showed high level correspondence with the presented experimental data. Starting with the results of the pressure drops, the overall mean relative errors are limited to 15 %, and this validates our use of the CFD experiments to build a pressure loss surrogate model. However, some deviation is noted for the development of the solid concentration profile along the diameter of the pipe. Roughly speaking, the validity of the mathematical model under the given range conditions is proven, and these results will allow us to construct pressure loss laws. Finally, a surrogate model is tested, which makes it possible to predict the pressure drops as a function of the variation in the solid concentration without performing simulations. Further tests are to come where greater variation in parameters such as solids concentration, particle size and even pipe diameter will be taken into account to increase result's accuracy. This type of surrogate models can be incorporated for plant's operators to predict pressure drops as a function of the variation of different flow parameters. However, Further simulations are now required to account for enough wide range conditions to cover different types of applications in several industries, including phosphate slurries.

Acknowledgement

This work was supported by "Office Chérifien des Phosphates" (OCP Group) Morocco.

Bibliography

A. Akhtar, V. Pareek, and M. Tadé. Cfd simulations for continuous flow of bubbles through gas-liquid columns: Application of vof method. *Chemical Product and Process Modeling*, 2, 01 2007.

M. A. Al-Yaari and B. F. Abu-Sharkh. Cfd prediction of stratified oil-water flow in a horizontal pipe. *Asian Transactions on Engineering*, 1(5):68–75, 2011.

C. L. Antaya, K. F. K. Adane, and R. S. Sanders. Modelling concentrated slurry pipeline flows. 44755: 1659–1671, 2012.

S. K. Arolla and O. Desjardins. Transport modeling of sedimenting particles in a turbulent pipe flow using euler–lagrange large eddy simulation. *International Journal of Multiphase Flow*, 75:1 – 11, 2015.

R. Askey and J. A. Wilson. *Some basic hypergeometric orthogonal polynomials that generalize Jacobi polynomials*, volume 319. American Mathematical Soc., 1985.

T. R. Auton, J. C. R. Hunt, and M. Prud'Homme. The force exerted on a body in inviscid unsteady non-uniform rotational flow. *Journal of Fluid Mechanics*, 197:241–257, 1988.

M. Berveiller. Eléments finis stochastiques: approches intrusive et non intrusive pour des analyses de fiabilité. 2005.

M. Berveiller, B. Sudret, and M. Lemaire. Stochastic finite element: a non intrusive approach by regression. *European Journal of Computational Mechanics/Revue Européenne de Mécanique Numérique*, 15(1-3):81–92, 2006.

X. Bin and S. DaWen. Applications of computational fluid dynamics (CFD) in the food industry: a review. *Computers and Electronics in Agriculture*, 34, 2002.

B. M. Bossio, A. J. Blanco, and F. H. Hernandez. Eulerian-eulerian modeling of non-newtonian slurries flow in horizontal pipes. 43727:525–533, 2009.

J. Capecelatro and O. Desjardins. Eulerian–lagrangian modeling of turbulent liquid–solid slurries in horizontal pipes. *International Journal of Multiphase Flow*, 55:64–79, 10 2013.

N. F. Carnahan and K. E. Starling. Equation of state for nonattracting rigid spheres. *The Journal of Chemical Physics*, 51:635–0, 1969.

J. Chauchat, Z. Cheng, T. Nagel, C. Bonamy, and T.-J. Hsu. Sedfoam-2.0: A 3-d two-phase flow numerical model for sediment transport. *Geoscientific Model Development*, 10:4367–4392, 11 2017.

L. Chen, Y. Duan, W. Pu, and C. Zhao. Cfd simulation of coal-water slurry flowing in horizontal pipelines. *Korean Journal of Chemical Engineering*, 26:1144–1154, 07 2009.

C. T. Crowe, J. D. Schwarzkopf, M. Sommerfeld, and Y. Tsuji. *Multiphase flows with droplets and particles*. CRC press, 2011.

A. M. DeGennaro, C. W. Rowley, and L. Martinelli. Uncertainty quantification for airfoil icing using polynomial chaos expansions. *Journal of Aircraft*, 52(5):1404–1411, 2015.

C. Dinescu, S. Smirnov, C. Hirsch, and C. Lacor. Assessment of intrusive and non-intrusive non-deterministic cfd methodologies based on polynomial chaos expansions. *International Journal of Engineering Systems Modelling and Simulation*, 2(1-2):87–98, 2010.

A. Doucet, N. De Freitas, and N. Gordon. *An introduction to sequential Monte Carlo methods*. Springer, 2001.

D. A. Drew and S. L. Passman. *Theory of multicomponent fluids*, volume 135. Springer Science & Business Media, 2006.

J. Dufek and G. W. Bergantz. Suspended load and bed-load transport of particle-laden gravity currents: the role of particle–bed interaction. *Theoretical and Computational Fluid Dynamics*, 21:119–145, 03 2007.

K. Ekambara, R. S. Sanders, K. Nandakumar, and J. H. Masliyah. Hydrodynamic simulation of horizontal slurry pipeline flow using ansys-cfx. *Industrial & Engineering Chemistry Research*, 48:8159–8171, 09 2009.

M. Elkarii, C. Bouallou, and A. Ratnani. Towards modelling a diphasic flow using the CFD technique to achieve a digital twin of a Phosphate slurry piping process. *Chemical Engineering Transactions*, 81:757–762, 2020.

R. G. Ghanem and P. D. Spanos. *Stochastic finite elements: a spectral approach*. Courier Corporation, 2003.

D. Gidaspow. Multiphase flow and fluidization: Continuum and kinetic theory descriptions by d. gidaspow. *The Canadian Journal of Chemical Engineering*, 73:784–784, 1994.

R. G. Gillies, C. A. Shook, and J. Xu. Modelling heterogeneous slurry flows at high velocities. *The Canadian Journal of Chemical Engineering*, 82, 2004.

J. González, N. Sabirgalieva, L. Rojas-Solorzano, and G. Zarruk. Numerical simulation of slurry flows in heterogeneous and saltation regimes in horizontal pipelines. *Chemical Engineering Transactions*, 57:1279–1284, March 2017.

M. K. Gopaliya and D. Kaushal. Modeling of sand-water slurry flow through horizontal pipe using cfd. *Journal of Hydrology and Hydromechanics*, 64(3):261 – 272, 2016.

M. K. Gopaliya and D. R. Kaushal. Analysis of effect of grain size on various parameters of slurry flow through pipeline using cfd. *Particulate Science And Technology*, 10 2015.

S. A. Hashemi, R. B. Spelay, K. F. K. Adane, and R. Sean Sanders. Solids velocity fluctuations in concentrated slurries. *The Canadian Journal of Chemical Engineering*, 94:1059–1065, 06 2016.

F. H. Hernandez, A. J. Blanco, and L. Rojas-Solorzano. Cfd modeling of slurry flows in horizontal pipes. 48401:857–863, 2008.

C. M. Hrenya and J. L. Sinclair. Effects of particle-phase turbulence in gas-solid flows. *AIChE Journal*, 43:853–869, 1997.

A. Jahedi and G. Ahmadi. Application of wiener-hermite expansion to nonstationary random vibration of a duffing oscillator. 1983.

Y. Jiang and P. Zhang. Numerical investigation of slush nitrogen flow in a horizontal pipe. *Chemical Engineering Science*, 73:169–180, 2012.

Y. Jiang and P. Zhang. Pressure drop and flow pattern of slush nitrogen in a horizontal pipe. *AIChE Journal*, 59:1762–1773, 05 2013.

L. Jing, C. Y. Kwok, Y. F. Leung, and Y. D. Sobral. Extended cfd-dem for free-surface flow with multi-size granules. *International Journal for Numerical and Analytical Methods in Geomechanics*, 40: 62–79, 01 2016.

D. Kaushal, T. Thinglas, Y. Tomita, and S. K. H. Tsukamoto. Cfd modeling for pipeline flow of fine particles at high concentration. *International Journal of Multiphase Flow*, 43:85–100, 2012.

N. Kumar, M. K. Gopaliya, and D. Kaushal. Experimental investigations and cfd modeling for flow of

highly concentrated iron ore slurry through horizontal pipeline. *Particulate Science and Technology*, 37(2):232–250, 2017.

S. Lahiri and K. Ghanta. Regime identification of slurry transport in pipelines: A novel modelling approach using ann & differential evolution. *Chemical Industry and Chemical Engineering Quarterly*, 16:329–343, 2010.

M. Li, Y. He, Y. Liu, and C. Huang. Effect of interaction of particles with different sizes on particle kinetics in multi-sized slurry transport by pipeline. *Powder Technology*, 09 2018a.

M.-z. Li, Y.-p. He, Y.-d. Liu, and C. Huang. Hydrodynamic simulation of multi-sized high concentration slurry transport in pipelines. *Ocean Engineering*, 163:691–705, 07 2018b.

C. Lin and M. Ebadian. A numerical study of developing slurry flow in the entrance region of a horizontal pipe. *Computers & Fluids*, 37:965–974, 2008.

J. Ling, P. Skudarnov, C. Lin, and M. Ebadian. Numerical investigations of liquid–solid slurry flows in a fully developed turbulent flow region. *International Journal of Heat and Fluid Flow*, 24:389–398, 2003.

C. Lun and S. Savage. The effects of an impact velocity dependent coefficient of restitution on stresses developed by sheared granular materials. *Acta Mechanica*, 63(1-4):15–44, 1986.

C. Lun, S. Savage, D. Jeffrey, and N. Chepurniy. Kinetic theories for granular flow: Inelastic particles in couette flow and slightly inelastic particles in a general flowfield. *Journal of Fluid Mechanics*, 140: 223 – 256, 03 1984.

M. R. Maxey and J. J. Riley. Equation of motion for a small rigid sphere in a nonuniform flow. *The Physics of Fluids*, 26(4):883–889, 1983.

G. V. Messa and S. Malavasi. Improvements in the numerical prediction of fully-suspended slurry flow in horizontal pipes. *Powder Technology*, 270:358–367, 01 2015.

G. V. Messa and V. Matoušek. Analysis and discussion of two fluid modelling of pipe flow of fully suspended slurry. *Powder Technology*, 9 2020.

G. V. Messa, M. Malin, and S. Malavasi. [asme asme 2013 pressure vessels and piping conference - paris, france (sunday 14 july 2013)] volume 4: Fluid-structure interaction - numerical prediction of pressure gradient of slurry flows in horizontal pipes. 2013.

G. V. Messa, M. Malin, and S. Malavasi. Numerical prediction of fully-suspended slurry flow in horizontal pipes. *Powder Technology*, 256:61–70, 04 2014.

H. N. Najm. Uncertainty quantification and polynomial chaos techniques in computational fluid dynamics. *Annual review of fluid mechanics*, 41:35–52, 2009.

T. N. Ofei and A. Y. Ismail. Eulerian-eulerian simulation of particle-liquid slurry flow in horizontal pipe. *Journal of Petroleum Engineering*, 2016:1–10, 2016.

T. N. Ofei, S. Irawan, and W. Pao. Cfd method for predicting annular pressure losses and cuttings concentration in eccentric horizontal wells. *Journal of Petroleum Engineering*, 2014:1–16, 2014.

A. Passalacqua and R. O. Fox. Implementation of an iterative solution procedure for multi-fluid gas–particle flow models on unstructured grids. *Powder Technology*, 213(1-3):174–187, 2011.

D. Pham Van Bang, E. Lefrançois, P. Sergent, and F. Bertrand. Expérimentation par irm et modélisation par éléments finis de la sédimentation-consolidation des vases. *La Houille Blanche*, pages 39–44, 06 2008.

A. Rabhi, A. Chkifa, S. Benjelloun, and A. Latifi. Surrogate-based modeling in flotation processes. *Computer Aided chemical engineering*, 43:229–234, 2018.

M. T. Reagana, H. N. Najm, R. G. Ghanem, and O. M. Knio. Uncertainty quantification in reacting-flow simulations through non-intrusive spectral projection. *Combustion and Flame*, 132(3):545–555, 2003.

Y. Seong, C. Park, J. Choi, and I. Jang. Surrogate model with a deep neural network toevaluate gas–liquid flow in a horizontal pipe. *Energies*, 13:968, 2020.

R. Silva, P. Faia, F. Garcia, and M. Rasteiro. Characterization of solid–liquid settling suspensions using electrical impedance tomography: A comparison between numerical, experimental and visual information. *Chemical Engineering Research and Design*, 111:223–242, 07 2016.

J. L. Sinclair and R. Jackson. Gas-particle flow in a vertical pipe with particle-particle interactions. *AIChE Journal*, 35:1473–1486, 1989.

M. K. Singh, S. Kumar, and D. Ratha. Computational analysis on disposal of coal slurry at high solid concentrations through slurry pipeline. *International Journal of Coal Preparation and Utilization*, 40(2):116–130, 2017.

S. A. Smolyak. *Quadrature and interpolation formulas for tensor products of certain classes of functions*, volume 148. Russian Academy of Sciences, 1963.

T.-C. Sun. A finite element method for random differential equations with random coefficients. *SIAM Journal on Numerical Analysis*, 16(6):1019–1035, 1979.

M. Syamlal, W. Rogers, and T. J. O'Brien. Mfix documentation theory guide. 12 1993.

A. Uzi and A. Levy. Flow characteristics of coarse particles in horizontal hydraulic conveying. *Powder Technology*, 12 2017.

H. K. Versteeg and W. Malalasekera. An introduction to computational fluid dynamics: the finite volume method. 2007.

J. Wang, S. Wang, T. Zhang, and Y. Liang. Numerical investigation of ice slurry isothermal flow in various pipes. *International Journal of Refrigeration*, 36, 1 2013.

C. Y. Wen and Y. H. Yu. A generalized method for predicting the minimum fluidization velocity. *AIChE Journal*, 12(3):610–612, 1966.

N. Wiener. The homogeneous chaos. *American Journal of Mathematics*, 60(4):897–936, 1938.

D. Xiu and G. E. Karniadakis. The wiener–askey polynomial chaos for stochastic differential equations. *SIAM journal on scientific computing*, 24(2):619–644, 2002.

D. Xiu and G. E. Karniadakis. Modeling uncertainty in flow simulations via generalized polynomial chaos. *Journal of computational physics*, 187(1):137–167, 2003.